

Immersed Boundary-Lattice Boltzmann Coupling Scheme for Fluid-Structure Interaction with Flexible Boundary

Yongguang Cheng¹, Hui Zhang^{2,*} and Chang Liu¹

¹ State Key Laboratory of Water Resources and Hydropower Engineering Science, Wuhan University, Wuhan 430072, China.

² School of Electrical Engineering, Wuhan University, Wuhan 430072, China.

Received 30 October 2009; Accepted (in revised version) 21 December 2010

Available online 18 February 2011

Abstract. Coupling the immersed boundary (IB) method and the lattice Boltzmann (LB) method might be a promising approach to simulate fluid-structure interaction (FSI) problems with flexible structures and complex boundaries, because the former is a general simulation method for FSIs in biological systems, the latter is an efficient scheme for fluid flow simulations, and both of them work on regular Cartesian grids. In this paper an IB-LB coupling scheme is proposed and its feasibility is verified. The scheme is suitable for FSI problems concerning rapid flexible boundary motion and a large pressure gradient across the boundary. We first analyze the respective concepts, formulae and advantages of the IB and LB methods, and then explain the coupling strategy and detailed implementation procedures. To verify the effectiveness and accuracy, FSI problems arising from the relaxation of a distorted balloon immersed in a viscous fluid, an unsteady wake flow caused by an impulsively started circular cylinder at Reynolds number 9500, and an unsteady vortex shedding flow past a suddenly started rotating circular cylinder at Reynolds number 1000 are simulated. The first example is a benchmark case for flexible boundary FSI with a large pressure gradient across the boundary, the second is a fixed complex boundary problem, and the third is a typical moving boundary example. The results are in good agreement with the analytical and existing numerical data. It is shown that the proposed scheme is capable of modeling flexible boundary and complex boundary problems at a second-order spatial convergence; the volume leakage defect of the conventional IB method has been remedied by using a new method of introducing the unsteady and non-uniform external force; and the LB method makes the IB method simulation simpler and more efficient.

AMS subject classifications: 76M28, 74F10

Key words: Lattice Boltzmann method, immersed boundary method, fluid-structure interaction, flexible boundary, complex boundary.

*Corresponding author. *Email addresses:* chengyg2004@yahoo.com.cn (Y. Cheng), hzhang@whu.edu.cn (H. Zhang), bery11988@163.com (C. Liu)

1 Introduction

The immersed boundary (IB) method has been developing rapidly since it was first invented to simulate the heart valve flow by Peskin in 1972 [1]. Recently, it was viewed as a general method for computer simulations of biological systems interacting with fluids [2], and the successful simulations of three-dimensional human heart flows [3–5], insect flight [6], aquatic animal locomotion [7, 8], filament flapping dynamics [9, 10], blood cell aggregation [11, 12], biofilm processing [13] and parachute dynamics [14, 15] have exhibited its great potential and profound perspective. However, the existing versions of the IB method have some inadequacies, within which the solution of the fluid equations is not efficient enough and needs to be improved [16]. Because the IB method's fluid equations must be solved in a regular Cartesian grid, one may think of taking the lattice Boltzmann (LB) method as a substitute for the original spectral or finite-difference fluid flow scheme. The LB method [17] is a regular lattice-based scheme for fluid flow simulation, and its simplicity, efficiency, parallelism and aptness for many fluid flow problems have been extensively verified [17–23]. The fact that both the IB method and the LB method work on a regular grid or lattice makes the IB-LB coupling possible. Moreover, the superiority of the LB method for fluid flow simulation may improve the IB method's efficiency.

An IB-LB coupling scheme might be promising for simulating fluid-structure interaction (FSI) and moving boundary problems. Some preliminary but successful attempts have been conducted [10–12, 24–28]. Feng in 2004 first published an IB-LB coupled scheme for simulating particle-fluid interaction problems [24]. Later, Peng upgraded the scheme by using a multi-block lattice and a multi-relaxation-time LB scheme to enhance stability and to implement local grid refinement [25]. Shu improved the convergence of the coupling scheme by correcting the velocity to enforce the physical boundary conditions [26]. Dupuis simulated the flow past an impulsively started cylinder [27]. Niu improved the calculation of the boundary force on the fluid [28]. The above works were aimed at rigid body-fluid interaction, and most of them used the flow past a cylinder or buoyant particles as the simulation example. On the other hand, for flexible boundary FSI simulations by the IB-LB coupling, Zhang studied the red blood cell aggregation process [11, 12] and Zhu proposed a 3D scheme for the sheet flapping phenomenon [10], showing profound perspective of the approach. To date, only a few works on the IB-LB coupled scheme for problems with flexible structures have been available.

This paper presents an IB-LB coupled scheme for flexible structure-fluid interaction and complex boundary problems. It is the preparation for the future 3D simulation of the human heart dynamics. The merits of the scheme are that it is suitable for rapid moving boundary and large pressure gradient FSI problems, and the volume leakage is relatively small. These will be verified by simulating typical problems. In the second section, the concepts of the IB and LB methods and the detailed coupling algorithm will be described. In the third section, three flow phenomena, respectively caused by the oscillating relaxation of a distorted balloon, the impulsive startups of a circular cylinder

and a rotating cylinder are simulated. The discussion and conclusions will be in the fourth and fifth sections.

2 The IB-LB coupling scheme

2.1 The IB method for flexible immersed boundaries

2.1.1 The idea and formulation of the IB method

In the IB method, an Eulerian description of the Navier-Stokes (N-S) equations is used for the fluid dynamics, and a Lagrangian description of curvilinear boundary structural mechanics is used for objects immersed in the fluid. The immersed boundary is assumed to consist of massless fibers, so that all of the force generated by distortions of the boundary can be calculated easily and transmitted directly to the fluid. A 2D example with a single closed immersed boundary fiber (curve) is shown in Fig. 1(a). The boundary curve and the fluid domain are denoted by Γ_b and Ω_f , respectively. Lowercase letters are used for Eulerian variables, while uppercase letters are used for Lagrangian variables. Thus, $\mathbf{X}(s,t)$ is a Lagrangian vector function of arc length s (in some reference configuration) and time t , giving the location of points on Γ_b . The boundary effect is modeled by a singular Lagrangian force $\mathbf{F}(s,t)$ at the boundary point $\mathbf{X}(s,t)$. $\mathbf{F}(s,t)$ is determined by the configuration of $\mathbf{X}(s,t)$ and it is properly transferred into the Eulerian forcing term \mathbf{f} in the N-S equations. The N-S equations are solved to determine the flow velocity and pressure throughout the fluid domain Ω_f . The immersed boundary moves at the local fluid flow velocity since it is in contact with the surrounding fluid, while the flow velocity on the boundary is consistent with the non-slip boundary condition. This scheme may be governed by the following set of equations:

$$\frac{\partial \rho}{\partial t} + \nabla \cdot (\rho \mathbf{u}) = 0, \quad (2.1a)$$

$$\frac{\partial (\rho \mathbf{u})}{\partial t} + \nabla \cdot (\rho \mathbf{u} \mathbf{u}) = -\nabla p + \nu \nabla \cdot [\rho (\nabla \mathbf{u} + (\nabla \mathbf{u})^T)] + \mathbf{f}, \quad (2.1b)$$

$$\frac{d\mathbf{X}(s,t)}{dt} = \mathbf{U}(\mathbf{X}(s,t), t) = \int_{\Omega_f} \mathbf{u}(\mathbf{x}, t) \delta(\mathbf{x} - \mathbf{X}(s,t)) d\mathbf{x}, \quad (2.1c)$$

$$\mathbf{F}(s,t) = \mathcal{S}_f \mathbf{X}(s,t), \quad (2.1d)$$

$$\mathbf{f}(\mathbf{x}, t) = \int_{\Gamma_b} \mathbf{F}(s,t) \delta(\mathbf{x} - \mathbf{X}(s,t)) ds, \quad (2.1e)$$

where \mathbf{u} is the flow velocity, \mathbf{U} the boundary speed, ρ the fluid density, p the flow pressure, ν the fluid kinematic viscosity, \mathbf{x} the fluid flow coordinate, \mathbf{X} the boundary coordinate, s the boundary fiber length, \mathcal{S}_f the boundary force generation operator, and $\delta(\mathbf{r})$ the Dirac delta function. Eqs. (2.1a) and (2.1b) are the Navier-Stokes equations with external force \mathbf{f} in Eulerian form for the fluid flow, while Eqs. (2.1c) and (2.1d) are the immersed boundary dynamic equations in Lagrangian form for the boundary. The left

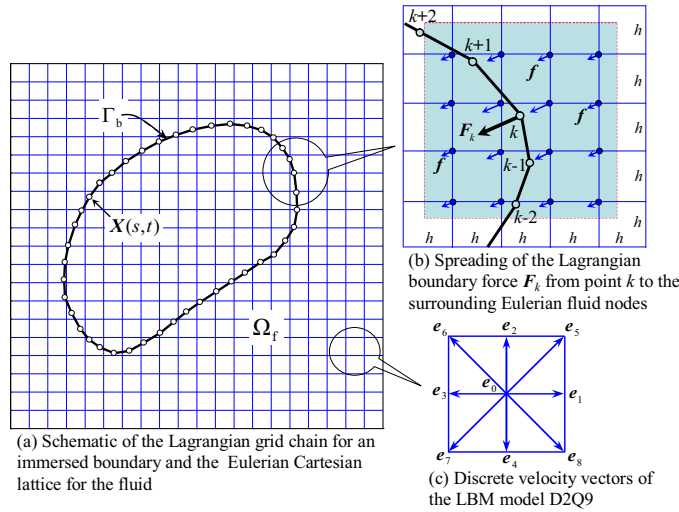


Figure 1: Schematic of the coupling idea of the immersed boundary method and the lattice Boltzmann method.

part of Eq. (2.1c) describes the boundary kinematics. Eq. (2.1d) denotes the constitutive law of modeling the force F , which is generated from the configuration of the immersed boundary due to its elasticity, with S_f being problem-dependent. Eq. (2.1e) and the right part of Eq. (2.1c) are the interaction equations of fluid and boundary, with the former for spreading the Lagrangian force to the Eulerian force and the latter for imposing the flow velocity on the boundary to obtain the boundary speed \mathbf{U} . The interaction is realized by using the coupling kernel, namely an integral operation on the Dirac delta function $\delta(\mathbf{r})$.

2.1.2 The discrete form of the interaction equations

The above equations are solved on a pair of computational grids: a cell-centered uniform Cartesian grid for the Eulerian fluid flow variables and a discrete chain of points for the Lagrangian boundary variables. As a 2D example in Fig. 1, the coordinates of the i, j -th Eulerian grid node are $x_{ij} = ((i + 1/2)\Delta x, (j + 1/2)\Delta y)$ ($i = 0, 1, \dots, n; j = 0, 1, \dots, m$), assuming the lower left corner of the domain is the origin. Thus \mathbf{u}_{ij} denotes the value of \mathbf{u} at x_{ij} . The Lagrangian grid-points are identified by a single index k ($k = 0, 1, \dots, n_b$). Thus F_k denotes the value of F at the k -th grid-point \mathbf{X}_k .

The interaction between fluid nodes and boundary grid-points, governed by the integration against the Dirac delta function in the continuous Eqs. (2.1c) and (2.1e), is handled by introducing a regularized discrete delta function δ_h . The discretized forms of Eqs. (2.1c) and (2.1e), by using δ_h , may be expressed as

$$f_{ij} = \sum_k F_k \delta_h(\mathbf{x}_{ij} - \mathbf{X}_k) \Delta s_k, \tag{2.2a}$$

$$\frac{d\mathbf{X}_k}{dt} = \mathbf{u}_k = \sum_{i,j} \mathbf{u}_{ij} \delta_h(\mathbf{x}_{ij} - \mathbf{X}_k) \Delta x \Delta y, \tag{2.2b}$$

where $h = \Delta x = \Delta y$ is the fluid node spacing and Δs_k is the length of the k -th fiber segment.

Theoretically, $\Delta s_k \leq h/2$ is necessary to guarantee the non-slip boundary condition and to prevent fluid leakage across the boundary [16].

2.1.3 The discrete delta function

The discrete delta function δ_h appearing in Eqs. (2.2a) and (2.2b) is a smoothed approximation to the Dirac delta function $\delta(r)$. The detailed derivation procedures and several forms were presented in literature [16]. We apply the common form as follows:

$$\delta_h(x,y) = \frac{1}{h^2} \phi\left(\frac{x}{h}\right) \phi\left(\frac{y}{h}\right), \tag{2.3a}$$

$$\phi(r) = \begin{cases} \frac{1}{8}(3-2|r| + \sqrt{1+4|r|-4r^2}), & 0 \leq |r| < 1, \\ \frac{1}{8}(5-2|r| - \sqrt{-7+12|r|-4r^2}), & 1 \leq |r| < 2, \\ 0, & |r| \geq 2. \end{cases} \tag{2.3b}$$

The stencil width of $\phi(r)$ is $4h$, and its profile is shown in Fig. 2.

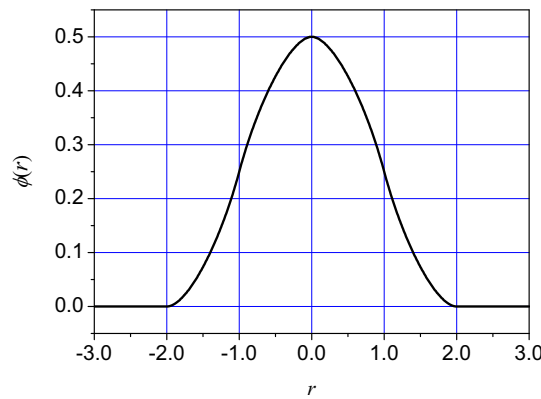


Figure 2: The profile of the regularized delta function $\phi(r)$.

2.1.4 Fluid-boundary interaction

Fig. 1(b) is a graphical representation of the force transformation from a single IB point \mathbf{X}_k to the nearby fluid nodes. Since the force at an IB point contributes to the Eulerian force density over a $4h \times 4h$ square area in the discrete Eq. (2.2a), the integral operation is known as the force spreading operation. Eq. (2.2a) defines the fluid force f_{ij} at node x_{ij} as being calculated by the spreading effect from boundary forces F_k at all IB points \mathbf{X}_k ($k = 0, 1, \dots, n_b$). However, because the stencil width of δ_h is $4h$, as defined in (2.3b), the Eulerian force density f_{ij} is affected only by the force F_k confined within $|\mathbf{X}_k - \mathbf{x}_{ij}| \leq 2$. On the other hand, Eq. (2.2b) is a simple interpolation operation and works much like the spreading operator but in reverse, and it defines the speed \mathbf{U}_k at an IB point \mathbf{X}_k by fluid velocities \mathbf{u}_{ij} at all fluid nodes x_{ij} ($i = 0, 1, \dots, n; j = 0, 1, \dots, m$). Again, only the velocities

u_{ij} of the 16 nearest nodes ($|\mathbf{X}_k - \mathbf{x}_{ij}| \leq 2$) contribute to the boundary grid-point speed \mathbf{U}_k . Fig. 1(b) could almost be reused as a depiction of Eq. (2.2b) as well, but the interpolated field at the IB point would be an average of the surrounding values, instead of being much bigger than all of them. Therefore, though the summation operations of Eqs. (2.2a) and (2.2b) are on all boundary grid-points and fluid nodes, only those within the stencil width have nonzero influence. In other words, the interaction is locally defined in the immersed boundary scheme.

2.1.5 Boundary force calculation

The boundary force F is defined by the fiber configuration. For the fiber with tension, bending and fastening forces, Eq. (2.1d) can be practically expressed as

$$F = k_c \frac{\partial^2 \mathbf{X}}{\partial s^2} - k_\gamma \frac{\partial^4 \mathbf{X}}{\partial s^4} - k_f (\mathbf{X} - \mathbf{Z}), \quad (2.4)$$

in which k_c is the fiber tension stiffness, k_γ the fiber bending rigidity, k_f the fastening stiffness, and \mathbf{Z} the fastening or target position of the fiber.

When discretized along the fiber arc length, Eq. (2.4) may be expressed in the finite difference form:

$$F_k = k_c \left(\frac{\mathbf{X}_{k-1} - 2\mathbf{X}_k + \mathbf{X}_{k+1}}{\Delta s^2} \right) - k_\gamma \left(\frac{\mathbf{X}_{k-2} - 4\mathbf{X}_{k-1} + 6\mathbf{X}_k - 4\mathbf{X}_{k+1} + \mathbf{X}_{k+2}}{\Delta s^4} \right) - k_f (\mathbf{X}_k - \mathbf{Z}_k). \quad (2.5)$$

After the fiber forces F_k ($k = 0, 1, \dots, n_b$) at fiber points are known, one can use Eq. (2.2a) to calculate the forces that the boundary exerts on the fluid. Then, it is the task of the LB method to solve the N-S equations with an external forcing term.

2.2 The LB method for fluid flow

The LB method operates on a regular lattice and decomposes the fluid domain into a set of lattice nodes. The fluid is modeled as a group of fluid particles that are only allowed to move between lattice nodes or stay at rest. The composition of the lattice nodes depends on the chosen lattice model. The most common lattice model for two-dimensional simulations is the one using a square lattice with nine discrete velocity directions (denoted as model D2Q9, shown in Fig. 1(c)), while the three-dimensional model normally uses a cubic lattice with fifteen discrete velocity directions (model D3Q15) [17].

The motion of fluid particles is governed by the discrete lattice Boltzmann equation. For problems with a body force, the common LB equation with Bhatnagar-Gross-Krook (BGK) collision operator is

$$f_\alpha(\mathbf{x} + \mathbf{e}_\alpha \Delta t, t + \Delta t) - f_\alpha(\mathbf{x}, t) = -\frac{1}{\tau} [f_\alpha(\mathbf{x}, t) - f_\alpha^{eq}(\mathbf{x}, t)] + \Delta t g_\alpha(\mathbf{x}, t), \quad (2.6)$$

where f_α is the particle velocity distribution function along the α -th particle velocity direction, f_α^{eq} the equilibrium distribution function, g_α the forcing term function, τ the relaxation factor, \mathbf{e}_α the discrete particle vector, \mathbf{x} the lattice grid, and Δt the time increment.

Fig. 1(c) shows the discrete particle vectors $e_\alpha (\alpha=0,1,2,\dots,8)$ for model D2Q9. The three-dimensional fifteen particle model D3Q15 has fifteen discrete particle vectors, namely $e_\alpha (\alpha=0,1,2,\dots,14)$. The equilibrium distribution functions are based on variables ρ, \mathbf{u} and e_α , by defining [17]

$$f_\alpha^{eq} = w_\alpha \rho \left[1 + 3(e_\alpha \cdot \mathbf{u}) + \frac{9}{2}(e_\alpha \cdot \mathbf{u})^2 - \frac{3}{2}|\mathbf{u}|^2 \right], \tag{2.7}$$

where the weighting parameters are

$$w_\alpha = \begin{cases} \frac{4}{9}, & \alpha=0, \\ \frac{1}{9}, & \alpha=1,2,3,4, \\ \frac{1}{36}, & \alpha=5,6,7,8, \end{cases}$$

for D2Q9 and

$$w_\alpha = \begin{cases} \frac{2}{9}, & \alpha=0, \\ \frac{1}{9}, & \alpha=1,2,\dots,6, \\ \frac{1}{72}, & \alpha=7,8,\dots,14, \end{cases}$$

for D3Q15 in [17].

The macroscopic variables, namely the fluid density ρ and flow velocity \mathbf{u} , are defined in terms of the moments of the mesoscopic variable $f_\alpha(\mathbf{x},t)$ by

$$\rho(\mathbf{x},t) = \sum_\alpha f_\alpha(\mathbf{x},t), \quad \rho(\mathbf{x},t)\mathbf{u}(\mathbf{x},t) = \sum_\alpha e_\alpha f_\alpha(\mathbf{x},t). \tag{2.8}$$

The simulation procedures of the LB method are repeating the following steps: first, use (2.7) to calculate f_α^{eq} ; second, evolve (2.6) to obtain f_α ; third, calculate ρ and \mathbf{u} by (2.8); and then insert ρ and \mathbf{u} into (2.7) to get f_α^{eq} again.

Eq. (2.6) or a similar equation, along with $g_\alpha = 3w_\alpha f \cdot e_\alpha$, is widely accepted, and they are applied in [24–28]. Yet the introduction of the external forcing term by $\Delta t g_\alpha$ only has first-order convergence because f_{ij} is unsteady or non-uniform. For the problems concerning rigid or slowly moving boundaries or a flexible boundary with small pressure gradient, the first-order forcing introduction does not affect the global results. But for a fast moving boundary or a flexible boundary with a large pressure gradient, a higher order method is needed. To improve the accuracy of introducing the forcing term, Cheng presented a second-order convergence scheme [29], where the LB equation changes to

$$\begin{aligned} & f_\alpha(\mathbf{x} + e_\alpha \Delta t, t + \Delta t) - f_\alpha(\mathbf{x}, t) \\ &= -\frac{1}{\tau} [f_\alpha(\mathbf{x}, t) - f_\alpha^{eq}(\mathbf{x}, t)] + \frac{\Delta t}{2} [g_\alpha(\mathbf{x}, t) + g_\alpha(\mathbf{x} + e_\alpha \Delta t, t + \Delta t)], \end{aligned} \tag{2.9}$$

with forcing term function g_α being expressed as

$$g_\alpha = w_\alpha \{ A + 3\mathbf{B} \cdot [(e_\alpha - \mathbf{u}) + 3(e_\alpha \cdot \mathbf{u})e_\alpha] \}, \tag{2.10}$$

in which A is the source term in the fluid continuity equation and B is the external forcing term for the momentum equation. For Eqs. (2.1a) and (2.1b) here, we can just let $A = 0$ and $B = f$.

The LB model using Eqs. (2.9) and (2.10) has second-order accuracy for spatial resolution of fluid flow with unsteady and non-uniform source and forcing terms, which is consistent with the original LB model's accuracy. The second-order nature comes from the central-difference expression of the forcing term in (2.9) and the second-order term $(e_\alpha \cdot u)e_\alpha$ in (2.10). Because Eq. (2.9) is implicit, owing to the occurrence of the term $g_\alpha(x + e_\alpha \Delta t, t + \Delta t)$, an iterative procedure should be used at each time step. Normally, convergent results can be reached within several cycles.

2.3 Coupling procedures

Fig. 1 shows the basic concepts of the new coupling idea. We use the LB method to solve the fluid equations, namely the N-S Eqs. (2.1a) and (2.1b), use the force formula (2.5) to calculate the boundary force, use the fluid node external force formula (2.2a) to spread the boundary force to the fluid, and use formula (2.2b) to interpolate the speeds of the boundary points from the velocities of the nearby fluid nodes. The exact procedures are depicted in Fig. 3.

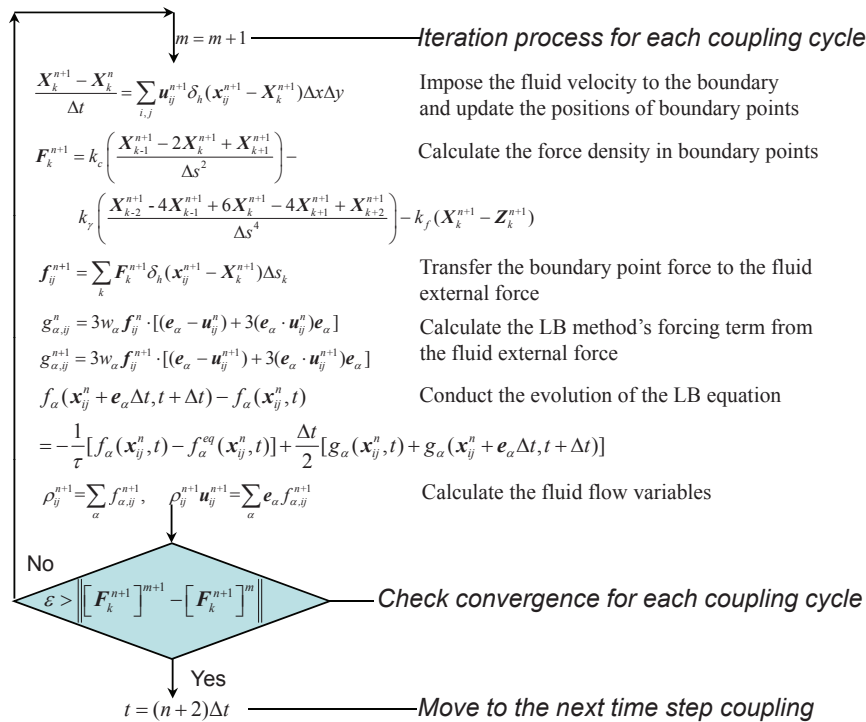


Figure 3: Coupling procedures of the IB-LB coupled scheme in a coupling cycle.

In every coupling cycle, an iteration process is needed because the scheme is semi-implicit. Numbered by m , the iteration ends when the convergence check is satisfied. Each iteration includes the following steps:

1. Impose the fluid velocity on the boundary and update the position of boundary point to \mathbf{X}_k^{n+1} by using formula (2.2b);
2. Calculate the force density \mathbf{F}_k^{n+1} at the boundary points by using formula (2.5);
3. Spread the boundary point force \mathbf{F}_k^{n+1} to the fluid external force \mathbf{f}_{ij}^{n+1} by using formula (2.2a);
4. Calculate the LB method's external forcing terms $g_{\alpha,ij}^n$ and $g_{\alpha,ij}^{n+1}$ from fluid external forces \mathbf{f}_{ij}^n and \mathbf{f}_{ij}^{n+1} by using formula (2.10);
5. Perform the evolution of the LB equation (Eq. (2.9)) to obtain the distribution functions $f_{\alpha,ij}^{n+1}$;
6. Calculate the fluid flow variables \mathbf{u}_{ij}^{n+1} by formula (2.8);
7. Compare the boundary point force \mathbf{F}_k^{n+1} at iteration step $m+1$ with that at iteration step m to check the convergence.

If the convergence check is satisfied, then the calculation moves to the next coupling cycle.

3 Scheme verification

3.1 Relaxation of a distorted balloon

To verify the effectiveness and accuracy of the proposed scheme, we compute a rapidly moving flexible boundary problem considered by [31, 32], where a 2D distorted balloon immersed in an incompressible fluid relaxes to its circular equilibrium shape. It may be an appropriate benchmark case for both the immersed interface method (IIM) [31, 32] and the IB method, because it is related to rapid boundary motion and large pressure gradient, and most importantly, the measurement of volume leakage is very convenient. In this example, a balloon is first distorted to a flower shape and the initial velocity and pressure inside and outside it are assumed to be zero. When the balloon is released, the balloon contraction drives the fluid to oscillate. The fluid flow and the balloon motion are fully coupled. At the final equilibrium, the velocity will attenuate to zero and the inside and outside pressures approach piecewise constant with a jump across the wall. Slightly different from [31, 32] where the fluid is incompressible and the number of flower leaves is five, we consider a weakly compressible fluid and a distorted six-leaf flower-shaped balloon in this case.

The distorted initial shape of the balloon is expressed in the cylindrical coordinates (r, θ) as

$$r(\theta) = r_0[1 + \varepsilon \cos(k\theta)], \quad 0 \leq \theta \leq 2\pi,$$

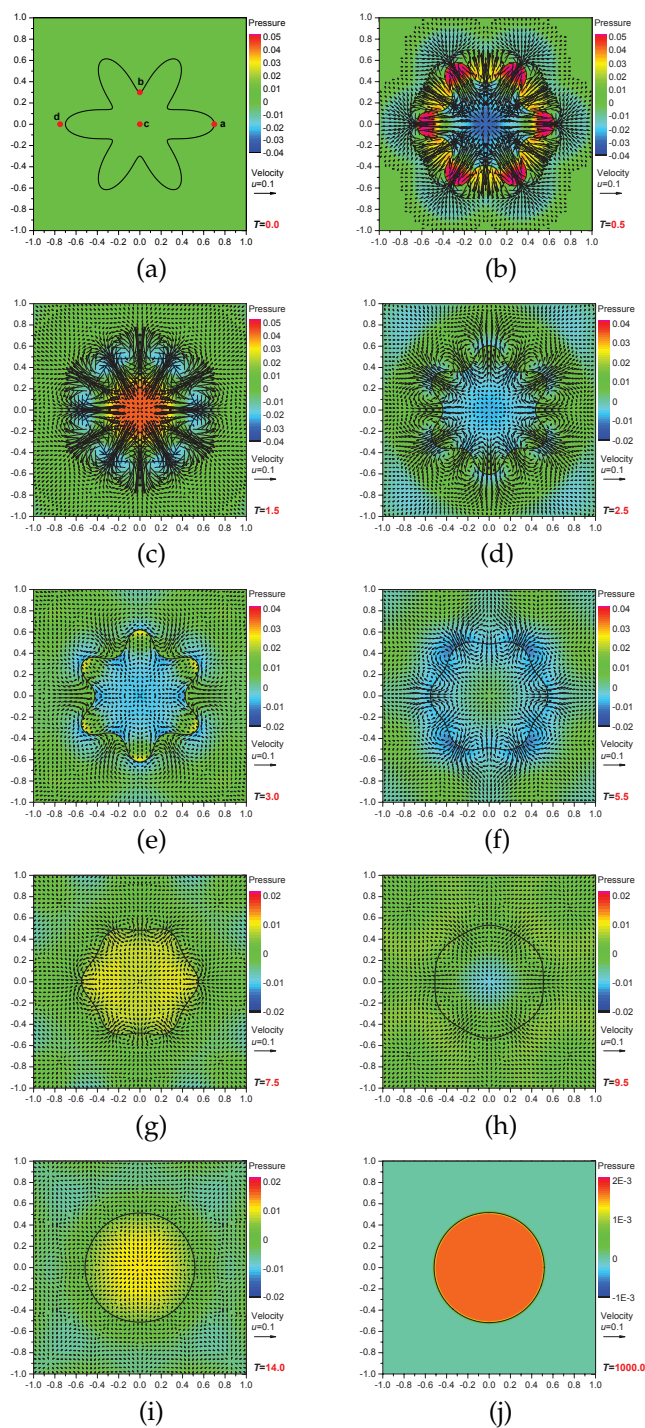


Figure 4: Velocity vectors and pressure distribution patterns induced by the relaxation of the distorted balloon at different times, simulated by 200×200 lattice. (a) $T=0.0$, (b) $T=0.5$, (c) $T=1.5$, (d) $T=2.5$, (e) $T=3.0$, (f) $T=5.5$, (g) $T=7.5$, (h) $T=9.5$, (i) $T=14.0$, (j) $T=1000.0$.

where r_0 , θ and k are constant, with k being the number of leaves. Here we choose $r_0=0.5$, $\varepsilon=0.4$ and $k=6$, thus the initial shape is that in Fig. 4(a). The initial enclosed area (or volume) is $A_i=r_0^2(1+0.5\varepsilon^2)\pi=0.848229$ and the initial perimeter (length) is $l_i=5.97229$. If we take the perimeter length at rest state (before distortion) to be $l_{rest}=0.5l_i=2.98615$, then, when the balloon relaxes to its equilibrium state, the radius, area and inside pressure should be $r_e=0.5182599$, $A_e=0.843811$, $p_e=0.001745$, respectively. These are the analytical values with which the following numerical results are to be compared. Since no explicit analytical formula is available, some of these values are calculated from implicit analytical formulae by MathCAD.

We simulate this FSI problem on a $[-1,1] \times [-1,1]$ domain, with the initial velocity $\mathbf{u}(x,y)=0$ and initial pressure $p(x,y)=0$ on the whole field, and the pressure boundary condition $p_{side}=0$ at the four sides. The first simulation uses an $n \times m = 200 \times 200$ LB lattice to discretize the domain, and accordingly the $2r_0$ resolution is 100. The balloon boundary is discretized to $n_b = 2200$ points to ensure $\Delta s_k \leq h/2$. The properties for the balloon boundary are $k_c=1.0$, $k_\gamma=0.0$ and $k_f=0.0$, and for the fluid are $\nu=0.1$ and $\rho=1.0$. The largest instant Reynolds number is $Re_{max} = (2r_0 \times u_{max})/\nu = 100 \times 0.241/0.1 = 241$, in which the maximum velocity is measured during the relaxation process. To monitor the histories of flow and boundary parameters, some probe points are assigned. As shown in Fig. 4(a), points a and b are the particular points of the boundary, and points c and d are particular locations in the flow field.

Fig. 4 shows the velocity vectors and pressure distributions at typical times $T = 0.0, 0.5, 1.5, 2.5, 3.0, 5.5, 7.5, 9.5, 14.0$, and 1000.0 , in which the interaction process of the fluid and balloon is demonstrated. Fig. 5 shows the oscillating histories of the enclosed volume A within the balloon, the radii r_a and r_b of the boundary points a and b , and the pressure p_c at the center point c of the flow field. To integrate the flow patterns and parameter histories for better understanding of the physical process, the corresponding times in Fig. 4 are marked in Fig. 5. It is shown that the balloon contracting force firstly actuates the fluid flow, generating abrupt pressure differences across the boundary, and then the pressure gradients react to the boundary, additionally affecting the boundary motion and balloon shape. The convex boundary regions move inward while the concave boundary regions move outward. The exchanges of shape regions and the fluctuations of fluid flow demonstrate a strong fluid-structure interaction phenomenon. This phenomenon is a decaying periodic process, with the final steady state being the balance of the boundary force and the inner pressure. The details may be described as follows. When the balloon begins to relax, the boundary tension strongly pushes the resting fluid to flow rapidly inward in the convex regions and outward in the concave regions ($u_{xa,max} = u_{xa}|_{T=1.6} = -0.174$, $u_{yb,max} = u_{yb}|_{T=0.05} = 0.241$), generating abrupt pressure gradients across the boundary ($\Delta p|_{T=0.5} \approx 0.056$) and 12 vortices around the boundary (Fig. 4(b)). Accelerated by the pressure gradients, the fluid continues to flow in the former directions and inversely pushes the boundary to reverse these concave and convex shapes (Fig. 4(c), (d)). As the reverse motion continues, the boundary tension increases and begins to retard the fluid, forming apparent pressure gradients in the concave and convex regions, which are re-

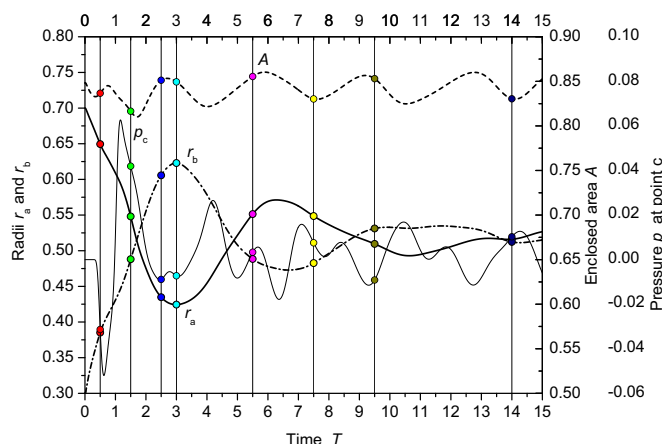


Figure 5: Oscillation histories of the radii, the enclosed volume and the center pressure during the early stage of the relaxation of the distorted balloon, simulated by 200×200 lattice.

verse to the initial concave and convex regions (Fig. 4(e)). The fluid and boundary interact in this manner, generating vivid regular vortex patterns and boundary shapes (Fig. 4(f), (g)). The interaction and oscillation attenuate gradually due to viscosity (Fig. 4(f), (g)) and finally reach the equilibrium state (Fig. 4(j)), in which the velocity is zero and the pressure has an abrupt jump between the inside and outside of the balloon.

Fig. 6 shows the pressure jump wire surface map at time $T = 1000.0$. It is apparent that the pressures both inside and outside the balloon are flat and smooth but the jump between them is sharp, with the transition region limited within the 4-lattice bandwidth.

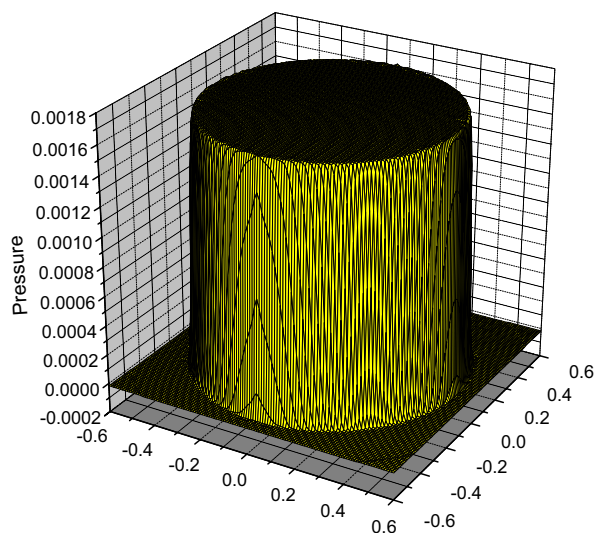


Figure 6: Pressure jump wire surface map of the balloon relaxation flow at time $T = 1000.0$, simulated by 200×200 lattice.

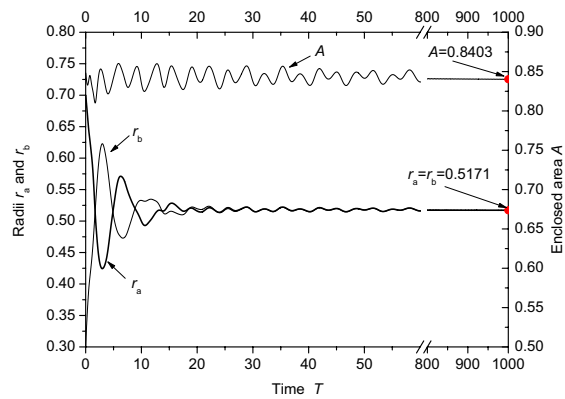


Figure 7: Long-range oscillation histories of the radii and enclosed volume of the relaxing balloon, simulated by 200×200 lattice.

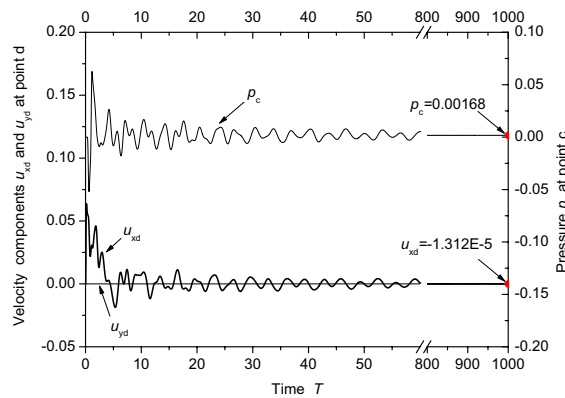


Figure 8: Long-range oscillation histories of the pressure and velocity of the relaxing balloon, simulated by 200×200 lattice.

Figs. 7 and 8 are the extension of Fig. 5. Fig. 7 depicts the long-range oscillating histories of r_a , r_b and A , while Fig. 8 exhibits the corresponding fluctuations of p_c , u_{xd} and u_{yd} , which are the velocity components at flow field point d . We know that the large scale oscillation, namely the exchanging motion between concave regions and convex regions, lasts several cycles until being damped around time $T = 30$, indicating the deformation process of the balloon shape. After $T = 30$, r_a and r_b oscillate with good synchronization, indicating the elastic contraction and relaxation process of the balloon. This wavy process gradually attenuates, and from time $T=800$ to 1000.0 all the boundary motion and fluid flow disappear. Figs. 7 and 8 also provide some near-equilibrium parameters, which are listed in Table 1 for comparison with the analytical solutions. From Table 1 we know that the numerical results agree very well with the analytical solutions, with the relative volume error less than 0.5%, the relative radius errors less than 0.3%, the relative pressure error less than 3.5%, and the velocity error less than $1.3E-5$, indicating a quite good volume conservation characteristic. The similar problem simulated by the

Table 1: Parameters of the relaxed balloon ($T=1000.0$) compared with analytical solutions.

Parameters	Area A	Radius $r_a=r_b$	Pressure p_c	Velocity u_{xd}
Simulated	0.8403	0.5171	0.00168	1.3e-5
Analytical	0.8438	0.5183	0.00174	0.000
Difference	0.41%	0.23%	3.45%	1.3e-5

Table 2: Spatial convergence analysis of balloon relaxation at time $T=2.0$.

Lattice for $2r_0$		100	200	300	400	500	600
Volume	$A _{T=2.0}$	0.82542	0.82603	0.82621	0.82629	0.82634	0.82638
	Error E_A	1.16E-3	4.13E-4	2.06E-4	1.06E-4	4.35E-5	0.0000
	Order	-1.4858	-1.7154	-2.31634	-3.9801		
Velocity	$u_{xd} _{T=2.0}$	0.04073	0.03982	0.03963	0.03954	0.03949	0.03946
	Error E_{ud}	3.20E-2	9.25E-3	4.19E-3	2.05E-3	8.34E-4	0.0000
	Order	-1.7945	-1.9524	-2.4865	-4.0288		
Pressure	$p_c _{T=2.0}$	0.00432	0.00330	0.00309	0.00301	0.00297	0.00294
	Error E_{pc}	4.67E-1	1.20E-1	5.05E-3	2.33E-2	8.92E-3	0.0000
	Order	-1.9638	-2.1302	-2.6960	-4.2961		

conventional IB method results in 10% level of volume leakage, and when improved by projection method, which needs much more computational effort, the value still remains above the 1% level [30,33,35]. These suggest that the current IB-LB coupling has valuable merits in volume conservation and computational efficiency.

To analyze the convergence feature, we keep the normalized parameters unchanged and refine the fluid lattice, boundary grid and time step. The values in Fig. 9 and Table 2 are taken at normalized time $T = 2.0$ by different fluid lattice and boundary grid resolutions. The relative errors, namely volume error E_A , velocity error E_{ud} at point d and

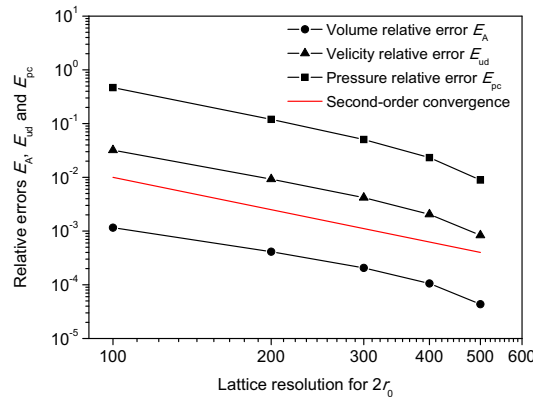


Figure 9: Spatial convergence characteristics of the IB-LB coupling scheme for the balloon relaxation flow (at time $T=2.0$), simulated by different lattice resolutions.

pressure error E_{pc} at point c , are defined based on the finest resolution of $2r_0 = 1.0$ by 600 lattice, owing to no analytical solution being available. The time $T=2.0$ is special because of being close to the time of the largest velocity or fastest boundary motion. Generally speaking, the second-order convergence is evident for volume conservation, velocity and pressure, consistent with the accuracy of the LB method. The higher convergence rates in large resolution cases, namely resolutions 400 and 500, are not the real rates because we substitute the values of resolution 600 for the analytical ones.

3.2 Flow past an impulsively started circular cylinder

The flow past an impulsively started circular cylinder is a benchmark case for verifying a numerical method's ability to treat curved complex boundary. In [27] the flow at Reynolds number 550 was simulated. Here we simulate the $Re = 9500$ case, which was studied both numerically and experimentally in [37]. We impose the non-slip boundary condition by fastening the IB boundary to the target position. The target position \mathbf{Z} in Eq. (2.4) is described as the circular cylinder. Given a very large fastening stiffness k_f , the IB boundary will approximate to the circular cylinder. The parameters for this case are Reynolds number $Re = 9500$, cylinder radius $r = 1$, far field uniform velocity $U_\infty = 1$, and kinematic viscosity $\nu = 2.10526E - 4$. The normalized time is defined as $T = U_\infty t / r$, where t is the actual time. We use a 2000×2000 lattice to simulate the whole flow field, locate the cylinder of 100 lattice in diameter at the center, discretize the IB boundary to $n_b = 644$ points, and set LB fluid flow properties $u = 0.1$, $\rho = 1000$, $\nu = 2.10526E - 3$ and boundary properties $k_c = 1000$, $k_\gamma = 1000$, $k_f = 10000$. The flow velocity within the cylinder is reset to 0 at every time step.

Fig. 10 demonstrates the streamline and pressure distribution patterns at different times $T = 1.2, 1.6, 2.0, 2.4, 2.8, 3.2, 3.6$ and 4.0 , in which the emergence and development of the so-called β and α vortices are vividly demonstrated. Fig. 11 gives two typical streamline patterns from literature [37], in which higher-order finite-difference schemes are used to solve the stream-function and vorticity formulae of the N-S equations. Our corresponding flow patterns are consistent with these accurate results. The pressure patterns show quite reasonable distributions with correct stagnation and focus points. Fig. 12 shows the main wake length variation curve compared with the experimental and numerical data of [37]. The present wake length values fit the experimental data despite of some small deviations, although not as good as the results of the higher-order finite-difference scheme. Generally speaking, our results of this $Re = 9500$ impulsively started circular cylinder flow agree well with the existing data, and the IB-LB scheme's effectiveness for fixed complex boundaries is successfully verified.

3.3 Flow past an impulsively started rotating cylinder

The flow past an impulsively started rotating cylinder is selected to verify the IB-LB scheme's ability for moving rigid boundary problems. The boundary treatments are sim-

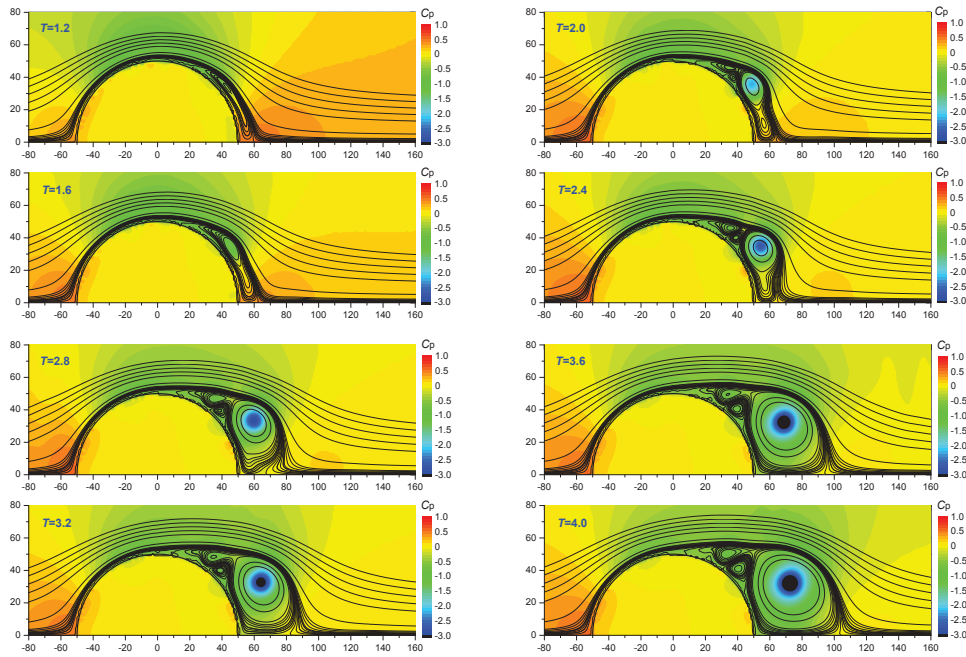


Figure 10: Flow patterns around the impulsively started circular cylinder at $Re = 9500$ and times $T=1.2, 1.6, 2.0, 2.4, 2.8, 3.2, 3.6$ and 4.0 . The coordinates are in the lattice unit.

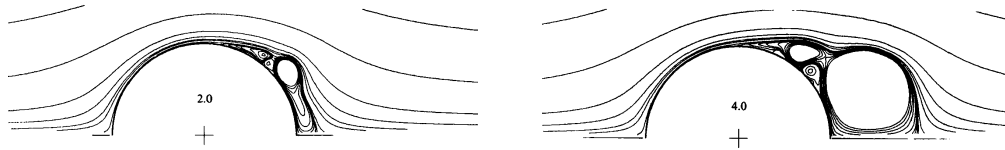


Figure 11: Flow patterns around the impulsively started circular cylinder at $Re = 9500$, times $T=2.0$ and 4.0 , adopted from reference [37].

ilar to that for the above $Re = 9500$ impulsively started circular cylinder. The only difference is that the target position Z is updated based on the rotating speed. The relative rotating speed is defined as $\alpha = r\omega/U_\infty$, where ω is the angular velocity of the cylinder about its axis. A 2000×2000 lattice for the flow field, the length of 25 lattice for the cylinder radius r , and $n_b = 451$ points for the boundary are applied. The properties for LB fluid flow are $u = 0.1$, $\rho = 1$ and $\nu = 0.005$, and for IB boundary are $k_c = 1$, $k_\gamma = 10$ and $k_f = 20$.

Fig. 13 presents the streamline patterns induced by an anticlockwise rotating cylinder with $Re = 1000$, $\alpha = 1$ at different times $T = 4.0, 7.0, 12.0$, and 16.0 . The generation and shedding of the wake vortex are clearly shown, which qualitatively agree with the existing simulated results such as Fig. 14 from [38].

This case suggests that our scheme is capable of simulating moving rigid boundary problems with large Reynolds number. For small Reynolds number problems, extensive verifications have been conducted in [24–28].

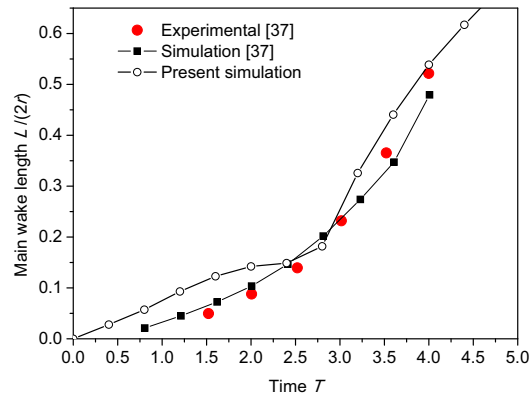


Figure 12: Wake length comparison with the existing numerical and experimental data for the impulsively started cylinder flow at $Re=9500$.

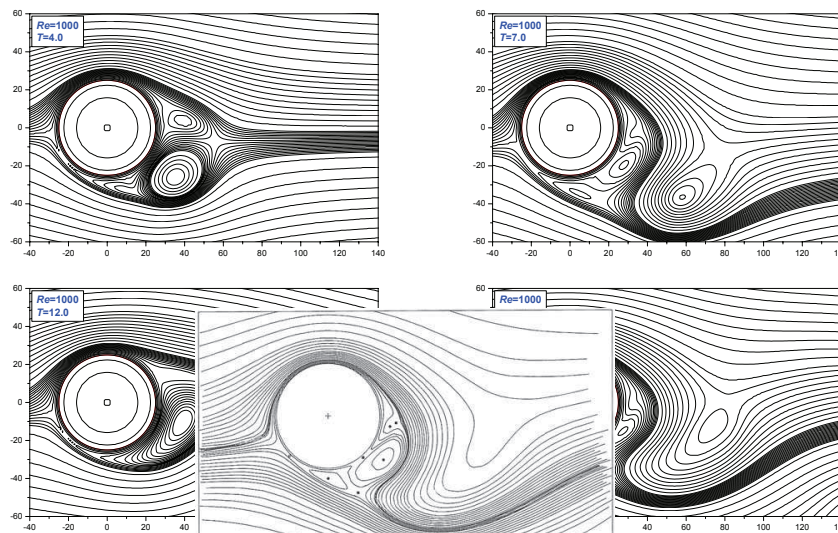


Figure 13: Flow patterns around the impulsively started rotating circular cylinder at $Re=1000$ and times $T=4.0, 7.0, 12.0$ and 16.0 . The coordinates are in the lattice unit.

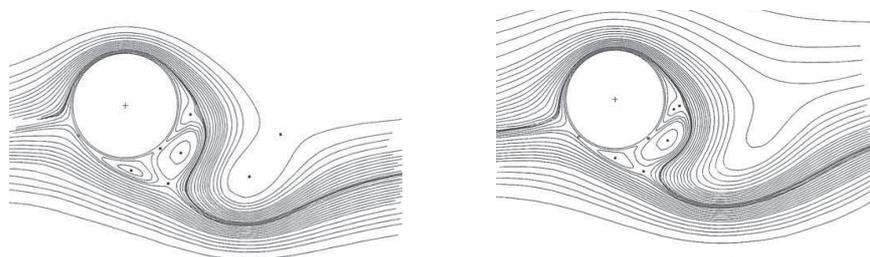


Figure 14: Flow patterns around the impulsively started rotating circular cylinder at $Re=1000$, times $T=7.0$ and 16.0 , adopted from reference [38].

4 Discussion

The LB method can promote the computational efficiency of the IB methods. This is partly because the finite-difference or spectral fluid flow solver in the conventional IB methods is not so efficient, partly because the projection calculation for reducing the volume leakage further increases the burden, and partly because the parallel computation of the LB method is much more efficient and easier to implement. These advantages have been demonstrated by [24–28] concerning rigid boundary flows, and by [10–12] concerning deformable and flexible boundary flows.

As stated in [16], the IB method has instability, volume leakage and near boundary error problems, which are dependent on the fluid solver and the discrete delta function. The instability hinders the simulation of problems with large boundary tension and pressure gradient across the boundary. The volume leakage affects the volume conservation in closed boundaries and the realization of the non-slip condition on the boundary, leading to a mismatch of fluid velocity and fiber speed. The fluid variables within the delta stencil width near the boundary can only achieve first-order spatial accuracy, even if the fluid solver is a high-order one, due to the first-order nature of the normal discrete delta functions [39, 40].

To simulate strong flexible boundary FSI problems and larger Reynolds number rigid boundary flows, the accuracy of boundary treatment, volume leakage and stability are all need to be improved. This paper demonstrates that the proposed IB-LB coupling scheme is suitable for these kinds of problems, because it can treat rapid boundary motion and large pressure gradient with quite good effects. Intensive and detailed analysis on coupling procedures, volume leakage and convergence is given, which is not available in the existing literature.

In this work, we find that the proposed IB-LB scheme with the new forcing term proposed in literature [29] is effective not only for minimizing the volume leakage and errors near the boundary, but also for improving stability. Compared with the existing IB methods, including the conventional IB method and the ones with volume conservation improvement, the volume leakage occurred in the present simulations is smaller if not the smallest, with only 0.41% for the balloon relaxation case here. The small volume leakage is very important for retaining the inside pressure of a closed boundary. Using the conventional IB method, the balloon will gradually shrink towards its rest state and the inside pressure will finally disappear (see the Fig. 8.5 in [33]). On the other hand, if the normal forcing term LB method is used (e.g., that in Eq. (2.6)), the balloon will gradually inflate (negative volume leakage) and the inside pressure will accordingly increase, and finally the balloon will burst owing to instability. Fig. 15 shows the volume histories by the normal forcing term, comparing with that by the new forcing term. It is evident that all simulations with the normal forcing term blow up before $T = 0.3$, a very early stage of the balloon relaxation. That is why we do not present the results by the normal forcing term LB method in the previous section. The negative volume leakage is proportional to the pressure gradients across the boundary, but the flux is from lower pressure region

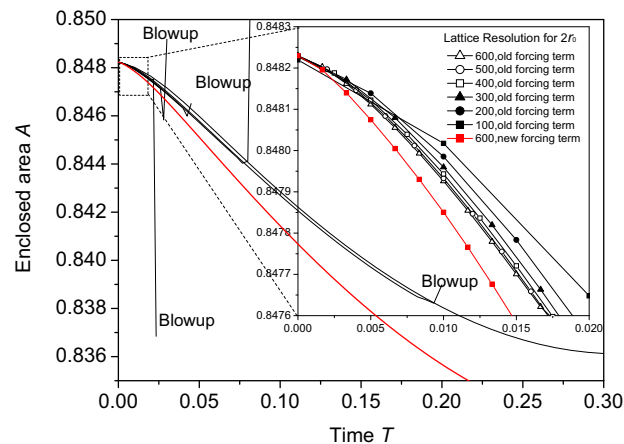


Figure 15: Comparison of the enclosed area histories between the normal forcing term LB model and the new forcing term LB model, showing the simulation blowups of the normal forcing term model with different lattice resolutions.

to higher pressure region. To simulate the large pressure jump problems, such as heart flow, the volume leakage effect should be carefully treated. However, when simulating open boundary [9, 10], rigid boundary [24–28] or small pressure jump [11, 12] problems, this negative volume leakage is negligible.

The forcing term in Eq. (2.9) gives second-order spatial and temporal convergence owing to its central-difference form, which has been verified in [29]. This is consistent with the LB method's second-order accuracy (when $\delta t / \delta x = c$ is fixed, the LB method is second-order both in space and time). In the balloon relaxation case, all the volume, velocity and pressure demonstrate second-order convergence characteristics in Fig. 9. Apart from the tiny volume and velocity errors, the pressure error being 3.45% after time $T=1000.0$ indicates quite good accuracy. The pressure jump between the inside and outside of the balloon is sharp with the transition width $4h$, which is consistent with the stencil width of the discrete Dirac delta function δ_h . Theoretically we cannot further sharpen the transition unless a narrow stencil width δ_h is used. We have tried 6 forms of δ_h in [16, 39], including the ones of $2h$ and $3h$ bandwidths, and concluded that Eq. (2.3b) is the best in terms of stability and accuracy. The stability of our scheme is relatively good. One reason may be that the second-order forcing term can combine the effects of the inside pressure and outside pressure across the pressure jump, while the normal forcing term separates the effects owing to the upwind nature. Another reason may be that the implicit iteration at every time step helps stabilize numerical oscillations.

Some further improvements should be made to the proposed scheme. The first one should be stability. Our experience shows that the scheme here has better stability than the normal IB-LB schemes, but is still unable to simulate the balloon relaxation with a Reynolds number larger than thousands. To simulate practical problems, such as the ventricular systole FSI, large boundary tension and pressure difference as well as fast flow velocity and boundary deformation need to be treated. On the other hand, the LB

method itself has stability problems in these fast transient situations. The LB model with a BGK collision operator used in this work is relatively weak, although it is simple. To further improve stability, the multi-relaxation-time LB scheme [34, 41] should be applied in future work. The second improvement should be avoiding fiber adherence. It is an open problem for all IB methods. If there are two or more fibers located in the same position or within the Dirac delta stencil width, it is very difficult to separate them. This problem occurs in simulations such as red blood cell aggregation and heart valve FSI problems, in which the boundaries (fibers) frequently come into contact. Because no effective method has been found so far, we just let the two boundaries stay apart beyond a distance of $2h$. The third one should be three-dimensional treatment of boundary mechanical formula. For the 2D problems such as the test cases here, using fiber to stand for boundary and formulating the boundary force by Eq. (2.4) are appropriate. However, when 3D curvature boundary surfaces need to be modeled, the existing fiber or fiber cluster depiction is not convenient. Therefore, a fiber network approach should be proposed and examined in future work.

5 Concluding remarks

This paper proposed an IB-LB coupling scheme for rapidly moving flexible boundary FSI problems. It is a preparation for modeling the heart flows similar to [3–5] in the future. The basic idea and detailed implementation procedures have been presented and the effectiveness has been verified. The novelty of the scheme comes from the better accuracy and stability and the ability to treat rapidly moving boundary and large pressure gradient across the boundary. These have been well verified by the successful simulation of the distorted balloon relaxation, in which the intensive quantitative analysis has been conducted. The scheme is also effective for complex rigid boundary flows, which was verified by the simulations of large Reynolds number impulsively started cylinder and rotating cylinder flows.

From this work we may conclude that (1) the LB method can properly work as the fluid flow solver in the IB method; (2) the proposed IB-LB coupling scheme has advantages in computational efficiency and volume conservation; (3) emphases should be laid on intensive accuracy analysis and stability improvement in the future; and (4) applying the scheme to more practical problems is also important for its further promotion.

Acknowledgments

This work is supported by the National Natural Science Foundation of China (NSFC, Grant numbers 10572106 and 10872153), the Scientific Research Foundation for Returned Overseas Chinese Scholars, Education Ministry, China, and the Program for New Century Excellent Talents in University (Grant number NCET-07-0628), Education Ministry, China.

References

- [1] C. S. Peskin, Flow Patterns Around Heart Valves: A Digital Computer Method for Solving the Equations of Motion, PhD thesis, Physiol., Albert Einstein Coll. Med., Univ. Microfilms., 378 (1972), 72–102.
- [2] C. S. Peskin, and D. M. McQueen, A General Method for the Computer Simulation of Biological Systems Interacting with Fluids—Biological Fluid Dynamics, ed. by C. P. Ellington et al., the Company of Biologists Limited, Cambridge, 1995.
- [3] D. M. McQueen, and C. S. Peskin, A three-dimensional computer model of the human heart for studying cardiac fluid dynamics, *Comput. Graphics.*, 34 (2000), 56–60.
- [4] J. D. Lemmon, and A. P. Yoganathan, Three-dimensional computational model of left heart diastolic function with fluid-structure interaction, *J. Biomech. Eng.*, 122 (2000), 109–117.
- [5] J. D. Lemmon, and A. P. Yoganathan, Computational modeling of left heart diastolic function: examination of ventricular dysfunction, *J. Biomech. Eng.*, 122 (2000), 297–303.
- [6] L. A. Miller, and C. S. Peskin, When vortices stick: an aerodynamic transition in tiny insect flight, *J. Exp. Biology.*, 207 (2004), 3073–3088.
- [7] R. Mitta, H. Dong, M. Bozkurttas, and A. Loebbecke, Analysis of flying and swimming in nature using an immersed boundary method, 36th AIAA Fluid Dynamics Conference and Exhibit, San Francisco, California, 2006.
- [8] L. J. Fauci, and C. S. Peskin, A computational model of aquatic animal locomotion, *J. Comput. Phys.*, 77 (1988), 85–108.
- [9] L. Zhu, and C. S. Peskin, Simulation of a flapping flexible filament in a flowing soap film by the immersed boundary method, *J. Comput. Phys.*, 179 (2002), 452–468
- [10] L. Zhu, G. He, S. Wang, L. Miller, X. Zhang, Q. You, and S. Fang, An immersed boundary method based on the lattice Boltzmann approach in three dimensions, with application, *Comput. Math. Appl.*, 2010, article in press, doi: 10.1016/j.camwa.2010.03.022.
- [11] J. Zhang, P. C. Johnson, and A. S. Popel, An immersed boundary lattice Boltzmann approach to simulate deformable liquid capsules and its application to microscopic blood flows, *Phys. Biol.*, 4 (2007), 285–295.
- [12] J. Zhang, P. C. Johnson, and A. S. Popel, Red blood cell aggregation and dissociation in shear flows simulated by lattice Boltzmann method, *J. Biomech.*, 41 (2008), 47–55.
- [13] R. Dillon, L. J. Fauci, A. L. Fogelson, and D. Gaver, Modeling biofilm processes using the immersed boundary method, *J. Comput. Phys.*, 129 (1996), 57–73.
- [14] Y. Kim, and C. S. Peskin, 2-D Parachute simulation by the immersed boundary method, *SIAM J. Sci. Comput.*, 28 (2006), 2294–2312.
- [15] Y. Kim, and C. S. Peskin, 3-D Parachute simulation by the immersed boundary method, *Comput. Fluids.*, 38 (2009), 1080–1090.
- [16] C. S. Peskin, The immersed boundary method, *Acta. Numer.*, 11 (2002), 479–517.
- [17] S. Chen, and G. D. Doolen, Lattice Boltzmann method for fluid flows, *Annu. Rev. Fluid. Mech.*, 30 (1998), 329–364.
- [18] H. W. Zheng, C. Shu, and Y. T. Chew, A lattice Boltzmann model for multiphase flows with large density ratio, *J. Comput. Phys.*, 218 (2006), 353–371.
- [19] C. X. Pan, L. S. Luo, and C. T. Miller, An evaluation of lattice Boltzmann schemes for porous medium flow simulation, *Comput. Fluids.*, 35 (2006), 898–909.
- [20] S. Chen, H. D. Chen, D. Martinez, and W. Matthaeus, Lattice Boltzmann model for simulation of magnetohydrodynamics, *Phys. Rev. Lett.*, 67 (1991), 3776–3779.
- [21] C. K. Aidun, and Y. N. Lu, Lattice Boltzmann simulation of solid particles suspended in

- fluid, *J. Stat. Phys.*, 81 (1995), 49–61.
- [22] R. Zhang, X. Shan, and H. Chen, Efficient kinetic method for fluid simulation beyond the Navier-Stokes equation, *Phys. Rev. E.*, 74 (2006), 046703.
- [23] Y. B. Gan, A. G. Xu, G. C. Zhang, X. J. Yu, and Y. Li, Two-dimensional lattice Boltzmann model for compressible flows with high Mach number, *Phys. A.*, 387 (2008), 1721–1732.
- [24] Z. G. Feng, and E. E. Michaelides, The immersed boundary-lattice Boltzmann method for solving fluid-particles interaction problems, *J. Comput. Phys.*, 195 (2004), 602–628.
- [25] Y. Peng, and C. Shu et al., Application of multi-block approach in the immersed boundary-lattice Boltzmann method for viscous fluid flows, *J. Comput. Phys.*, 218 (2006), 460–478.
- [26] C. Shu, N. Liu, and Y. T. Chew, A novel immersed boundary velocity correction-lattice Boltzmann method and its application to simulate flow past a circular cylinder, *J. Comput. Phys.*, 226 (2007), 1607–1622.
- [27] A. Dupuis, P. Chatelain, and P. Koumoutsakos, An immersed boundary-lattice Boltzmann method for the simulation of the flow past an impulsively started cylinder, *J. Comput. Phys.*, 227 (2008), 4486–4498.
- [28] X. D. Niu, C. Shu, Y. T. Chew, and Y. Peng, A momentum exchange-based immersed boundary-lattice Boltzmann method for simulating incompressible viscous flows, *Phys. Lett. A.*, 354 (2006), 173–182.
- [29] Y. G. Cheng, and J. P. Li, Introducing unsteady non-uniform source terms into the lattice Boltzmann model, *Int. J. Numer. Meth. Fluids.*, 56 (2008), 629–641.
- [30] C. S. Peskin, and B. F. Printz, Improved volume conservation in the computation of flows with immersed elastic boundaries, *J. Comput. Phys.*, 105 (1993), 33–46.
- [31] Z. L. Li, and M. C. Lai, The immersed interface method for the Navier-Stokes equations with singular forces, *J. Comput. Phys.*, 171 (2001), 822–842.
- [32] S. Xu, and Z. J. Wang, An immersed interface method for simulating the interaction of a fluid with moving boundaries, *J. Comput. Phys.*, 216 (2006), 454–493.
- [33] L. Lee, and R. J. LeVeque, An immersed interface method for incompressible Navier-Stokes equations, *SIAM J. Sci. Comput.*, 25 (2003), 832–856.
- [34] D. d’Humières, I. Ginzburg, M. Krafczyk, P. Lallemand, and L. S. Luo, Multiple-relaxation-time lattice Boltzmann models in three dimensions, *Philos. Trans. Royal. Soc. A.*, 360 (2002), 437–451.
- [35] E. P. Newren, Enhancing the Immersed Boundary Method: Stability, Volume Conservation and Implicit Solvers, PhD dissertation of The University of Utah, USA, 2007.
- [36] R. Mittal, and G. Iaccarino, Immersed boundary methods, *Annu. Rev. Fluid. Mech.*, 37 (2003), 239–261.
- [37] Ta Phuoc Loc, and R. Rouard, Numerical solution of the early stage of the unsteady viscous flow around a circular cylinder: a comparison with experimental visualization and measurements, *J. Fluid. Mech.*, 160 (1985), 93–117.
- [38] H. M. Badr, M. Coutanceau, and S. C. R. Dennis et al., Unsteady flow past a rotating circular cylinder at Reynolds numbers 10^3 and 10^4 , *J. Fluid. Mech.*, 220 (1990), 459–484.
- [39] B. E. Griffith, and C. S. Peskin, On the order of accuracy of the immersed boundary method: higher order convergence rates for sufficiently smooth problems, *J. Comput. Phys.*, 208 (2005), 75–105.
- [40] G. Le, and J. Zhang, Boundary slip from the immersed boundary lattice Boltzmann models, *Phys. Rev. E.*, 79(2) (2009), 026701.
- [41] P. Lallemand, and L. S. Luo, Theory of the lattice Boltzmann method: dispersion, dissipation, isotropy, Galilean invariance, and stability, *Phys. Rev. E.*, 61(6) (2000), 6546–6562.